Effects of electron cyclotron heating on the toroidal flow in LHD plasmas

Y. Yamamoto,[1, a)] S. Murakami,[1] C. C. Chang,[1] H. Takahashi,[2] K. Ida,[2] M. Yoshinuma,[2] and W. H. Ko[3]
[1)]*Department of Nuclear Engineering, Kyoto University, Kyoto 615-8540, Japan*
[2)]*National Institute of Fusion Science, Toki 509-5292, Japan*
[3)]*Korea Institute of Fusion Energy, Daejeon 34133, Republic of Korea*

(Dated: 30 July 2021)

The toroidal force related to electron cyclotron heating (ECH) is investigated in large helical device (LHD) plasmas. When we apply the ECH to the plasma kept by neutral beam injection (NBI) heating, the radial profile of the toroidal flow velocity changes drastically in LHD. ECH generated supra-thermal electrons can apply forces on the plasma through radial electron current and collisions. We investigate the perturbed electron distribution due to ECH by using the GNET code, which can solve the 5D drift kinetic equation. We also evaluate the electromagnetic force due to radial current and the collisional force driven by ECH. As a result, we find a comparable force driven by ECH to that by NBI heating. The direction of the force is the counter (co) direction radially inside (outside) from the ECH heating location, and these directions correspond with that of experiment results. Finally, we evaluate toroidal flows in ECH and NBI heated plasma solving the radial diffusion equation and compare them with that of experimental observations. We reproduce the co-rotating toroidal flow quantitatively in the balanced-NBI+ECH heated case, but we see a difference in the toroidal flow profiles in the co-NBI+ECH heated case.

I. INTRODUCTION

Many experiments suggest the important role of toroidal flow in turbulence transport. Recently, spontaneous toroidal flows have been observed in electron cyclotron heating (ECH) plasma in many tokamaks and helical devices such as JT-60U, Large Helical Device(LHD) and Helically Symmetric Experiment. It is necessary to clarify the underlying mechanism, and many experimental[1,2] and theoretical[3] studies have been undertaken to achieve this.

In LHD, toroidal flows have been investigated in the Neutral Beam Injection (NBI) heating and Electron Cyclotron Heating (ECH) plasmas, where the toroidal flow velocity of fully ionized carbon (C^{6+}) is measured by the charge exchange recombination spectroscopy (CXRS)[4,5]. It has been shown that the momentum diffusivity decreased with ion temperature increase in the ion internal transport barrier (ITB) core region, and spontaneous flows were identified[6–9]. The toroidal flows significantly changed when we applied ECH to the plasma kept by NBI heating. Figure 1 shows the change of the toroidal flow velocity of LHD experiments. In the case where balanced-NBI heating and on-axis ECH are applied, the toroidal flow increases gradually. The ECH is applied from $t = 4.1$s to 4.3s. At first, it starts to increase around $r/a \sim 0.3$ and gradually increases in the core later. Then, it gradually reaches the saturation, and the profile at $t = 4.29$s can be considered to be almost saturated in the experiment. In the case where co-NBI heating and off axis ECH are applied, the toroidal flow velocity decreases at the core region and increases outside of the ECH heating location. These results suggest that ECH should play a crucial role in the toroidal flow in LHD. However, the mechanism of the toroidal flow generation by ECH has not yet been understood well.

The driving force through $j_r \times B$ and collisions is one of the mechanisms for the toroidal flow generation. Some research focuses on the $j_r \times B$ and collisional forces by alpha heating, Ion Cyclotron Resonance Heating and perpendicularly injected NBI[10–13]. The forces by ECH has been considered to be small because the electron orbit width is small, although the orbit width can be large and ECH can generate the radial electron flux in a non-symmetric configuration such as a heliotron/stellarator[15]. Recently, it has shown that ECH could generate the finite driving force in non-symmetric configurations[14].

The $j_r \times B$ force is a consequence of return current in response to supra-thermal electrons' radial current generated by ECH. The momentum exchange between the supra-thermal electrons and the bulk plasma generates the collisional force. We consider that the $j_r \times B$ force has an important role in generating toroidal flow in non-axisymmetric helical devices. The $j_r \times B$ force and the collisional force do not cancel each other due to the breaking of the axisymmetry.

We evaluate the two forces driven by ECH using GNET code[15], which can solve a linearized drift kinetic equation in the 5D phase-space. We also compare the flow velocity obtained from the $j_r \times B$ and collisional forces with the observed flow velocity. In this paper, we investigate the driving force caused by ECH, not by the thermal bulk plasma behavior, because our target is to make clear the mechanism of the toroidal flow which changes by the presence or absence of ECH. Thus, we do not include the behavior of thermal bulk ions and electrons, which should be treated in the neoclassical theory. Also, we consider that the effect by the thermal plasma is small because the observed toroidal flows without ECH are negligible in LHD experiments.

The toroidal flows observed in the experiments have an asymmetry between inboard and outboard. It is considered as the Pfirsch-Schlüter flow effect[2,16–19]. We discuss the mean flow velocity, which is the average of the inboard and outboard flows, in this paper, so the asymmetric portion by the Pfirsch-Schlüter flow is not considered. Also, we consider that the effect of the ion bootstrap flow to the change of the toroidal

[a)]Electronic mail: yamamoto.yasuhiro@qst.go.jp;
The author's present affiliation is National Institutes for Quantum and Radiological Science and Technology, Rokkasho, Aomori 039-3212, Japan.

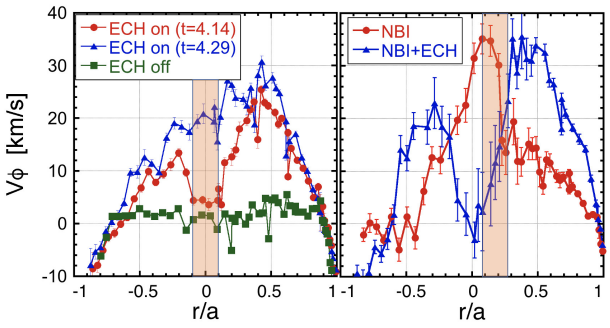

FIG. 1. The measured toroidal flow velocity in the balanced-NBI heating + on-axis ECH plasma (left) and the co-NBI heating + off-axis ECH plasma (right). The highlighted areas show the ECH absorption region. The ECH absorption profile is given in Fig. 7.

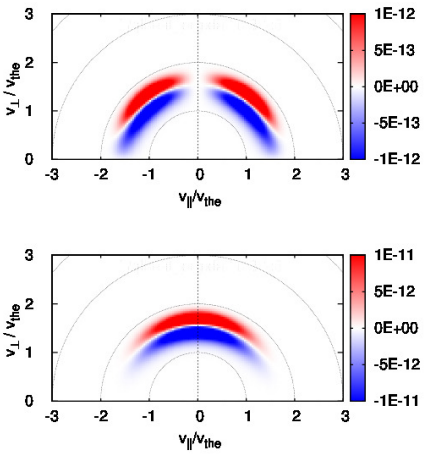

FIG. 2. The heating source using the quasi-linear diffusion theory of O-mode ECH (top) and X-mode ECH (bottom). $v_{\rm the}$ is the thermal velocity of 5keV.

flow would be small, and it is not included, neither. The bootstrap flow would contribute to the toroidal flow, but what we focus on is the change of the toroidal flow by ECH. The ion bootstrap flow is related to the ion temperature, ion pressure and the radial electric field[20]. However, these parameters observed in the target plasmas in this paper do not change greatly with/without applying ECH, although the electron temperature increases.

II. SIMULATION MODEL

To investigate the electron distribution function perturbed by ECH in the steady state, we apply the GNET code, which can solve the drift kinetic equation in 5-D phase space using the Monte Carlo method. We split the gyrophase averaged electron distribution function, f, into a stationary part, $f_{\rm Max}$, and an oscillating part by ECH, δf, as $f = f_{\rm max} + \delta f$, where we consider that the stationary part is Maxwellian. The drift kinetic equation for δf is given by

$$\frac{\partial \delta f}{\partial t} + (\mathbf{v}_d + \mathbf{v}_\parallel)\cdot\frac{\partial \delta f}{\partial \mathbf{r}} + \dot{v}\cdot\frac{\partial \delta f}{\partial \mathbf{v}} - C(\delta f) - L(\delta f) = S^{\rm ql}(f_{\rm max}) \qquad (1)$$

where $\mathbf{v}_\parallel$ and $\mathbf{v}_d$ are the velocity parallel to the magnetic field and the drift velocity, respectively. Also, $C(\delta f)$, $L(\delta f)$ and $S^{\rm ql}(f_{\rm max})$ are the collision operator, the orbit loss term, and the heating source term of ECH, respectively. The integration time is 2ms, which is long enough to follow the slowing down of the supra-thermal electrons.

The ECH source term is described by the quasi-linear diffusion theory. We consider only the linear effect $S^{\rm ql}(f_{\rm max})$ and ignore the quasi-linear effect $S^{\rm ql}(\delta f)$ for simplicity. Then the source term $S^{\rm ql}$ is given by

$$S^{\rm ql}(f_{\rm max}) = -\frac{\partial}{\partial v_i} D^{\rm ql}_{ij} \frac{\partial f_{\rm max}}{\partial v_j} \qquad (2)$$

where $D^{\rm ql}_{ij}$ is the quasi-linear diffusion tensor. The ECH deposition profile in the real space is obtained by ray-tracing. We consider that the right-handed electric field of the EC wave is dominant for X-mode, and the parallel component is dominant for O-mode. Under the limitations, we obtain[21,22]

$$S^{\rm ql}_{\rm X} = \frac{D^{\rm ql}_{\rm ECH}}{v_\perp}\frac{\partial}{\partial v_\perp}\left[v_\perp \left(\frac{v_\perp}{v_{the}}\right)^{2(n-1)} \times \delta(\omega - \frac{n\Omega_{ce}}{\gamma} - k_\parallel v_\parallel)\frac{\partial f_{\rm max}}{\partial v_\perp}\right] \text{ for X-mode} \qquad (3)$$

$$S^{\rm ql}_{\rm O} = \frac{D^{\rm ql}_{\rm ECH}}{v_\perp}\frac{\partial}{\partial v_\perp}\left[v_\parallel^2 v_\perp^{2n-1} \times \delta\left(\omega - \frac{n\Omega_{\rm ce}}{\gamma} - k_\parallel v_\parallel\right)\frac{\partial f_{\rm max}}{\partial v_\perp}\right] \text{ for O-mode,} \qquad (4)$$

where n, ω, $k_\parallel$, $\Omega_{\rm ce}$, γ and $D^{\rm ql}_{\rm ECH}$ are the harmonic number of the resonance, the wave frequency, the parallel wavenumber of the EC wave, the cyclotron frequency of electrons, the Lorentz factor of electrons, and the constant value, respectively. Both the fundamental O-mode and second harmonic X-mode are applied in the LHD experiments. Typical cases of the quasi-linear source term with parameters $k_\parallel = 0, n\Omega_{\rm ce}/\omega = 1.02, T_e = 5$keV are shown in Fig. 2, which means heating from the blue region to the red one in the velocity space. Here, the parameters $k_\parallel, n\Omega_{\rm ce}/\omega$ are important to determine the resonance condition $\omega = n\Omega_{\rm ce}/\gamma + k_\parallel v_\parallel$. Here, the Lorentz factor has velocity information, too. The O-mode ECH accelerates more passing electrons because Eq. 4 contains $v_\parallel$ explicitly, while the X-mode ECH accelerates more trapped electrons. Here, the strength of $S^{\rm ql}$ shown in the Fig. 2 cannot be compared between O-mode and X-mode because the parameter $D^{\rm ql}_{\rm ECH}$ is not included.

ECH applies forces on the plasma through $j \times B$ and collisions as below. Since the radial movements of energetic electrons accelerated by ECH are faster and larger than those of thermal electrons, ECH can drive the radial electron current $j_{\rm e}$. The net current in the steady state should vanish to

maintain the quasi-neutrality, so the return current, $j_r(=-j_e)$, must flow in the bulk plasma due to the ambipolar condition. Therefore, the bulk plasma feels $j_r \times B$ force due to the return current. The direction of the $j_r \times B$ torque by the outward (inward) electron flux is co (counter) direction because of the definition of co and counter, The co (counter) direction is defined such that the plasma current of co (counter) direction increases (decreases) the rotational transform determined by external coil currents and corresponds to the direction parallel (anti-parallel) to the toroidal magnetic field in LHD. On the other hand, the electrons drift toroidally due to the precession motion. During the slowing down of the energetic electrons, they transfer their momenta to the bulk plasma due to collisions. If we consider the isotropic source, the force of the particles passing in the co-direction should be equal to that of the particles passing in the counter-direction. The trapped particles, however, have precession motion, which can contribute to the net collisional force.

The $j_r \times B$ and collisional forces should cancel in the completely symmetric configuration in the symmetry direction[10,11]. Therefore, the conservation of angular momentum is satisfied and the total toroidal force should vanish in the axisymmetric configuration. However, non-symmetric magnetic modes enhance the radial electron flux and break the cancelation of the two forces. The non-symmetric component enhances the radial drift of energetic electrons, resulting in the relatively large radial diffusion of energetic electrons.

In the form of the Monte Carlo simulation, the toroidal component of the collisional force density, $F_\phi^{\rm col}$, is calculated as

$$F_\phi^{\rm col}(\rho_i) = R\sum_{n=1}^{n_{\rm max}} w_n \Delta p_{\parallel,n} \mathbf{b}\cdot\nabla\phi/\Delta V(\rho_i), \tag{5}$$

where ρ_i, R, ϕ, $\mathbf{b}$, ΔV, w_n and $\Delta p_{\parallel,n}$ are the normalized minor radius of the i-th radial grid, the major radius, the toroidal angle, the unit vector in the direction of the magnetic field, the volume of the i-th radial grid, the wight of the n-th test particle, which is determined by the ECH absorption power, and the change of the parallel momentum of the n-th test particle due to collisions, respectively. The summation is taken over the number of test particles in the i-th radial grid, $n_{\rm max}$. Also, the toroidal component of the $j_r \times B$ force is evaluated as

$$\begin{aligned} F_\phi^{j_r\times B}(\rho_i) &= j_r \times B_\theta \\ &= eB_\theta \sum_{n=1}^{n_{\rm max}} w_n \Gamma(\rho_i) \end{aligned} \tag{6}$$

where e, B_θ and Γ are the elementary charge, the poloidal magnetic field and the radial flux density due to δf of the i-th flux surface, respectively. Then, we refer to the driving force by ECH as $F_{\rm ECH}$, and

$$F_{\rm ECH} = F_{\phi,{\rm ECH}}^{\rm col} + F_{\phi,{\rm ECH}}^{j_r\times B}. \tag{7}$$

The force by NBI heating is evaluated with the FIT3D code[23], which is a module for NBI heating in TASK3D, the integrated transport code for helical plasmas[24–26]. The FIT3D code is the code which is similar to the GNET code. The prompt orbits of test particles are followed, and the finite orbit effects during the energy slowing down are not included because the orbit effect during the slowing down is considered to be small for the energetic ions injected by NBI heating. Tangential NBI ions give their momenta to the bulk plasma through collisions, as expressed in Eq. 5. Since it is considered that the collisional force is important as for NBI heating, we ignore the $j_r \times B$ force by NBI heating in this paper. We refer to the driving force by NBI heating as $F_{\rm NBI}$ and

$$F_{\rm NBI} = F_{\phi,{\rm NBI}}^{\rm col}. \tag{8}$$

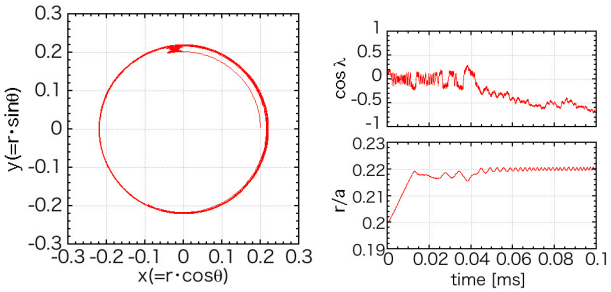

FIG. 3. The orbit calculation with pitch angle scattering and energy scattering. The poloidal projection of an electron orbit on the x-y plane (Left). The time development of the pitch angle $\lambda = v_\parallel/v$ and the normalized minor radius r/a (Right).

III. SIMULATION RESULTS

A. Behavior of supra-thermal electrons

Before we discuss the toroidal force by ECH, the orbit calculation including pitch angle scattering and energy scattering is performed. The pitch angle and position of an electron, which has the initial energy $E = 10$ keV and the initial pitch angle $\lambda = \cos 80°$, is shown in Fig. 3. The particle gets trapped soon due to pitch angle scattering. The radial drift of the trapped particle is significant, and it moves radially along the helical ripple. Due to the pitch angle scattering, it becomes a passing electron again, whose radial drift is smaller than trapped electrons. This is just a typical example, but trapped particles generally move more radially than passing particles.

Applying the GNET code, we evaluate the perturbed distribution function by ECH, δf, and the radial electron current enhanced by ECH in the steady state. We perform the simulations assuming the LHD plasma with inward shifted configuration ($R = 3.6$[m] and $B_t = 2.85$[T]), where the EC wave is X2-mode and the heating location is set at $r/a \sim 0.15$. Figure 4(a)-(c) shows the velocity distribution at $r/a \sim 0.0$, 0.15 and 0.25. They are integrated over the flux surface. Also, the velocity distribution integrated over the volume, total δf, is shown in Fig. 4(d). They show the deviation from the Maxwellian distribution, where the red (blue) region means the increase (decrease) of the distribution. It is found that

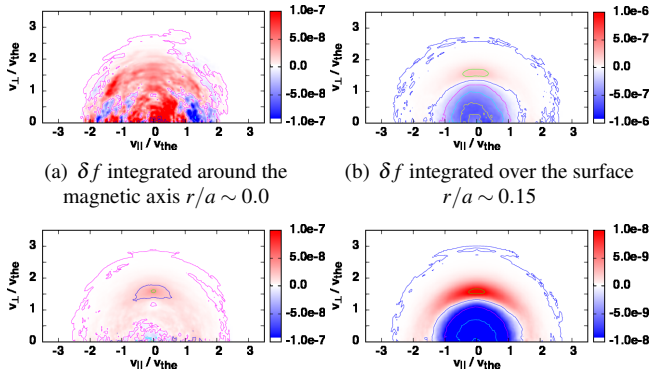

(a) δf integrated around the magnetic axis $r/a \sim 0.0$

(b) δf integrated over the surface $r/a \sim 0.15$

(c) δf integrated over the surface $r/a \sim 0.25$

(d) The total δf, which is integrated over the plasma volume.

FIG. 4. The deviations of the velocity distribution functions from Maxwellian, δf, which are integrated over the flux surface around (a) $r/a \sim 0.0$ (inside from the heating position), (b) $r/a \sim 0.15$ (around the heating position), and (c) $r/a \sim 0.25$ (outside from the heating position), and integrated over the whole volume (d).

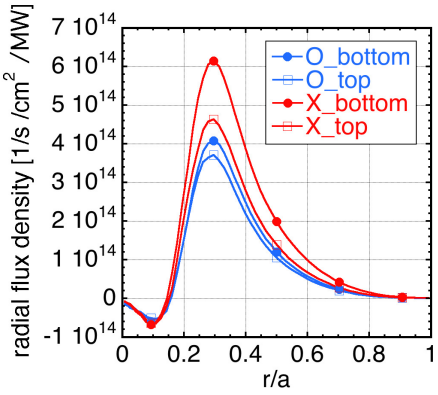

FIG. 5. The radial flux density of energetic electrons by O-mode and X-mode ECH per 1MW. The heating point is set at the ripple bottom ($\theta = 0^\circ, \phi = 18^\circ$) or the ripple top ($\theta = 180^\circ, \phi = 0^\circ$).

ECH decreases thermal electrons and makes a high energy tale, as shown in Fig. 4(d). The decreasing region is dominant around the heating point, and the growing region is dominant inside and outside from the heating point. It indicates that supra-thermal electrons heated by ECH enhance the electron flux from the heating point, and there is the resulting radial electron current.

We evaluate the polarization effect. As you can see, the heating source shown in Fig. 2, X-mode ECH generates more trapped electrons than O-mode ECH. Since trapped particles have a larger radial drift, we can expect that X-mode generates a larger radial flux of electrons than O-mode. The radial electron flux with O-mode and X-mode is shown in Fig. 5. It shows the dependence of the heating position, too. As we expected, the radial flux of X-mode is larger than that of O-mode. When the absorption of ECH is located at the magnetic ripple bottom ($r/a = 0.2, \theta = 0^\circ, \phi = 18^\circ$), more electrons get trapped. On the other hand, fewer electrons are trapped when absorption is located at the ripple top ($r/a = 0.2, \theta = 180^\circ, \phi = 0^\circ$). As you can see in Fig. 5, the ripple bottom heating makes the electron radial flux larger than that of the ripple top heating in both X-mode and O-mode cases. There is less difference in heating position in the O-mode case than that of the X-mode case. Because O-mode ECH source has less trapped particles, most supra-thermal electrons in the source term start as a passing particles, which does not move so radially. The passing particles can spread over the flux surface soon without large radial movement. After that, the passing electrons get trapped due to the pitch angle scattering and start to move radially. Thus the electron flux by O-mode ECH weakly depends on the heating position.

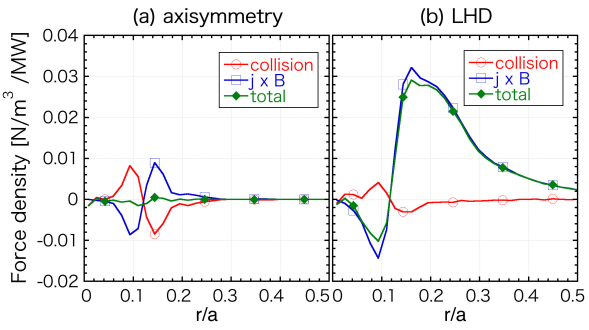

FIG. 6. The force density by ECH in (a) axisymmetric configuration and (b) LHD configuration per 1MW.

B. Toroidal force by ECH

As mentioned in Section 2, the $j_r \times B$ and collisional force cancel each other in a perfectly symmetric configuration. Figure 6 shows the $j_r \times B$ and collisional forces in an axisymmetric and the LHD configurations. The inward electron flux generates the counter-directed $j_r \times B$ force for the inner minor radii region ($r/a < 0.15$), and the outward electron flux generates the co-directed $j_r \times B$ force for the outer minor radii region ($r/a > 0.15$). We can see the cancelation in the axisymmetric configuration, which has similar parameters to LHD parameters, even though some portion due to finite orbit width still remained. However, we cannot see the cancelation any more in the LHD configuration. The non-symmetric magnetic modes enhance the electron flux, and they make more significant $j_r \times B$ force. The ECH force can drive the toroidal flow continuously while ECH is applied, because ECH generates the net force in the steady state.

We evaluate the toroidal forces with experimental parameters. We consider two typical cases: NBI(balanced)+ECH plasma with inward shifted configuration ($R = 3.6$[m], $B_t = 1.375$[T], discharge #129966), and NBI(Co)+ECH plasma with the inward shifted configuration ($R = 3.6$[m], $B_t = 2.85$[T], discharge #129235). Both plasmas are heated by tangential NBI and perpendicular NBI heating. The profiles of the electron density, the ion temperature and the electron temperature are shown in Fig. 8 and 9. The temperature and the

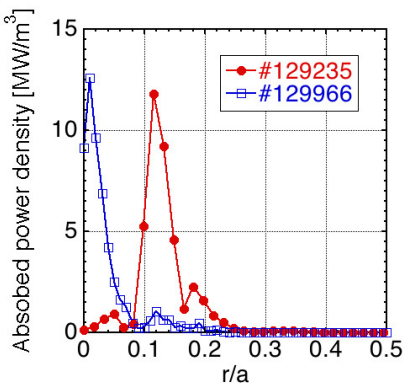

FIG. 7. The absorbed power density profiles obtained by ray-tracing code.

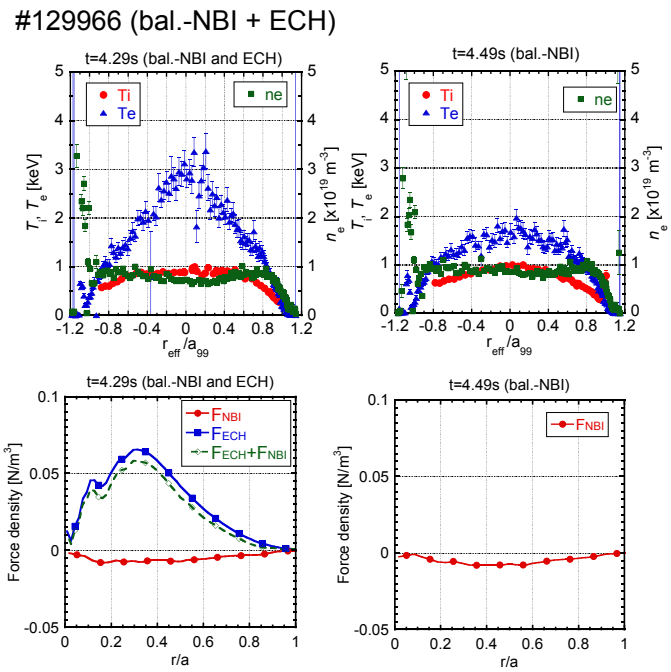

FIG. 8. The density and temperature profiles for the balanced NBI heating case #129966 at $t = 4.29$s (ECH is on) (top-left) and at $t = 4.49$s (ECH is off) (top-right). The force density profiles of $F_{\rm ECH}$ and $F_{\rm NBI}$ at $t = 4.29$s (bottom-left) and at $t = 4.49$s (bottom-right).

density are almost in the steady state at each selected time in Fig. 8 and 9.

In discharge #129966, three lines of X2-mode ECH are injected. The two of the ECH lines is almost on-axis heating and the other is off-axis heating. The absorbed power density is shown in Fig. 7. The toroidal force density driven by ECH and NBI heating is shown in Fig. 8 (bottom-left and bottom-right). The direction of the total force by ECH is the co direction, which is the same with that of the observed toroidal flow, because the heating location is almost center and there is

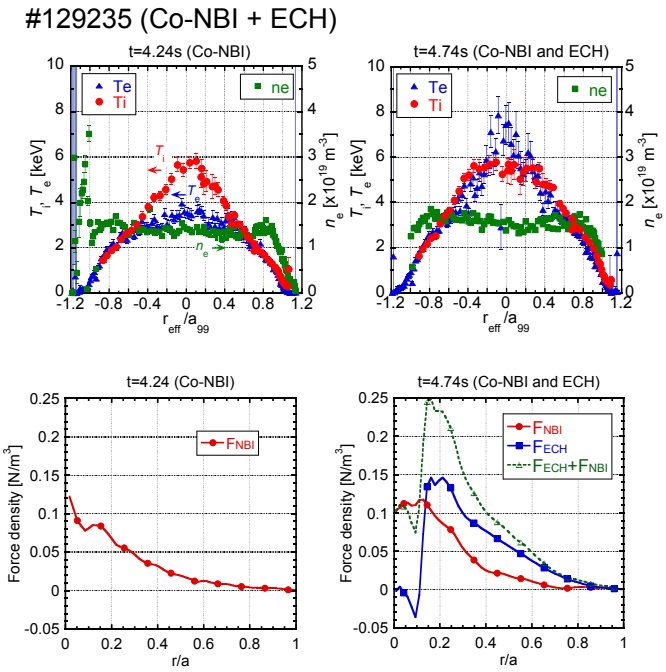

FIG. 9. The density and temperature profiles for the co NBI heating case #129235 at $t = 4.24$s (ECH is off) (top-left) and at $t = 4.74$s (ECH is on) (top-right). The force density profiles of $F_{\rm ECH}$ and $F_{\rm NBI}$ at $t = 4.24$s (bottom-left) and at $t = 4.74$s (bottom-right).

no inward electron flux driven by ECH. The momentum input from NBI heating is very small because of the balanced beam injection, and the force by ECH is much larger than that by the NBI heating. Also, the force by NBI heating weakly depends on the temperature profiles.

In discharge #129235, three lines of O1-mode ECH and two lines of X2-mode ECH are injected, and all of the five are off-axis heating. The absorbed power density is shown in Fig. 7. Also, all tangential NBI in LHD (#1, #2 and #3) are applied. NBI#1 and #3 are co-directed and NBI#3 is counter-directed in this shot and the total momentum input by NBI is co-directed. The toroidal force driven by ECH and NBI heating is shown in Fig. 9 (bottom-left and bottom-right). The direction of the force by off-axis ECH is counter (co) direction radially inside (outside) from the heating location. The negative peak and the positive peak appear on both sides of the power absorbed location because the inward and outward radial electron currents come up from the power deposition. The direction of the force qualitatively agrees with the change of toroidal flow velocity in the experiment as seen in the Fig. 1. We can see the ECH force can be comparable with the NBI force. The measured central electron temperature is about 3.5keV without ECH and about 7.0keV with ECH, and the measured central ion temperature is about 6keV regardless of the presence or absence of ECH. The different temperature profiles don't change the NBI force density, as well as the balanced NBI heating case.

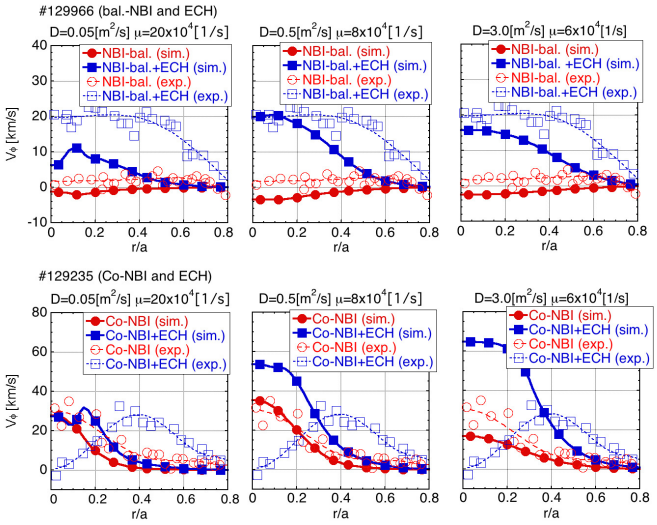

FIG. 10. Obtained toroidal flow velocities driven by ECH in the balanced NBI heating case #129966 with the coefficients $D = 0.05, \mu = 2\times10^5$(top-left), $D = 0.5, \mu = 8\times10^4$(top-center) and $D = 3, \mu = 6\times10^4$(top-right) and the co NBI heating case #129235 $D = 0.05, \mu = 2\times10^5$(bottom-left), $D = 0.5, \mu = 8\times10^4$(bottom-center) and $D = 3, \mu = 6\times10^4$(bottom-right). The solid lines are the simulation results and the dashed lines are the observed toroidal velocities.

C. Estimation of toroidal flow

The neoclassical viscosity is generally important for the toroidal flow in heliotron/stellarator plasmas. We evaluate the toroidal flow velocity in the steady state by solving momentum diffusion equation with the neoclassical toroidal viscosity

$$\frac{\partial m_i n_i V}{\partial t} = \frac{1}{r}\frac{\partial}{\partial r}\left(rD\frac{\partial m_i n_i V}{\partial r}\right) + F_{\rm NBI} + F_{\rm ECH} + F_{\rm NTV}, \tag{9}$$

where V, D, $F_{\rm NBI}$, $F_{\rm ECH}$ and $F_{\rm NTV}$ are the toroidal velocity, the radial diffusion coefficient and the force by NBI heating, ECH and neoclassical toroidal viscosity, respectively. For simplicity, we calculate the 1D diffusion equation. Here we consider the neoclassical toroidal viscosity is proportional to $(\delta B/B)^2$, and then it is simply evaluated as

$$F_{\rm NTV} = -m_i n_i \mu \left(\frac{\delta B}{B}\right)^2 V, \tag{10}$$

where $\delta B/B$ is the relative variation of the magnetic field strength and μ is the factor of proportionality, which is defined so that $\mu\cdot(\delta B/B)^2$ corresponds to the neoclassical toroidal viscosity coefficient. The radial diffusion coefficient is known as the perpendicular viscosity, and it is supposed to consist mostly of the anomalous perpendicular viscosity due to turbulence in the plasma. Also, we assume the one fluid plasma, that is, the hydrogen flow velocity is equal to that of fully ionized carbon, which is observed by CXRS. There is difference between hydrogen flow and impurity carbon flow in the neoclassical theory, but the difference of the toroidal flow would be small compared with the absolute value of the flow velocity[27,28].

We choose three sets of the parameters, $(D,\mu) = (0.05, 2\times10^5)$, $(0.5, 8\times10^4)$ and $(3.0, 6\times10^4)$. The viscosity coefficient $\mu\cdot(\delta B/B)^2$ with $\mu = 2\times10^5$ is consistent with that of Ref.[29]. However, the viscosity value with $\mu = 2\times10^5$ is too strong in the outer minor radii region ($r/a > 0.5$), as shown later. Thus, we add two parameters lower than expected. We note that the diffusion coefficient $D = 3.0$ is what we experimentally expect from Ref.[30] and $D = 0.05$ is smaller than the expected one. The purpose of this study is to clarify the effect of ECH driving force, so we select three sets of parameters (D,μ) so that the obtained flows in the Co-NBI heating case have agreed reasonably.

The obtained toroidal flows in the balanced NBI heating case are shown in Fig. 10. The obtained flows with $D = 0.5[\mathrm{m}^2/\mathrm{s}]$ and $\mu = 8\times10^4[1/\mathrm{s}]$ have good agreement with the experimental ones. The toroidal flow velocity is around zero with the balanced-NBI force, while the flow velocity can reach 20km/s with the additional ECH force. The toroidal flow without ECH shows the opposite direction compared with the observed one, though the difference is small because of the negative $F_{\rm NBI}$. It means that there would be another mechanism which is not included here, for example, the residual stress. With $D = 0.05[\mathrm{m}^2/\mathrm{s}]$ and $\mu = 2\times10^5[1/\mathrm{s}]$, the toroidal flow velocity is almost half of the measured flow velocity. As mentioned above, the toroidal flow in the outer minor radii region is strongly damped with $\mu = 2\times10^5[1/s]$, due to the neoclassical damping force. It might be due to the simple model of neoclassical viscosity. We have to note that the value of the toroidal velocity depends largely on the coefficients, and thus they have uncertainty.

The obtained toroidal flows in the co-NBI heating case are shown in Fig. 10. With smaller diffusion coefficient ($D = 0.05$), the flow velocity decreases inside of the EC heating point and increases outside. With larger diffusion coefficient ($D = 0.5$ and 3.0), however, the toroidal flow velocity increases over the entire minor radius, because the surrounding plasma drags the center of the plasma at $r/a \sim 0.2$, where the ECH force drives the toroidal flow in the co-direction. They cannot reproduce the velocity profiles completely in the co-rotating plasma.

One of the possible mechanisms for the toroidal flow generation mechanism is the change of the radial electric field E_r. The enhancement of the radial flux would cause the modification of the neoclassical ambipolarity. However, the observed radial electric field does not change so largely, as shown in Fig. 11. Also, the change of E_r is partially positive and partially negative in the case of #129966. It seems not to be consistent with the enhancement of the toroidal flow over the entire minor radius. Although the error bar of E_r for #129235 is large, the change of E_r is quite small. Therefore, we cannot explain the toroidal flow generation by the change of E_r.

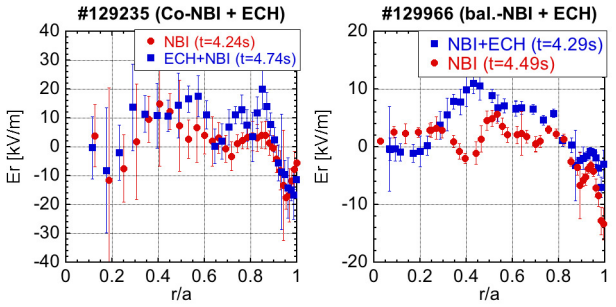

FIG. 11. The radial electric field profiles observed with CXRS.

IV. CONCLUSIONS

We have evaluated the $j_r \times B$ and collisional forces by ECH using the GNET code in order to clarify the mechanism of the toroidal flow change in LHD. We found that the $j_r \times B$ and collisional forces cancel each other in the axisymmetric configuration. In contrast, the $j_r \times B$ force is significant in the LHD configuration due to the breaking of the axisymmetry. Moreover, the radial electron current by ECH can be affected by the polarization of the EC wave and the heating position, because they are related to the fraction of trapped particles. The obtained $j_r \times B$ force can be the same order as the NBI force, and its direction agrees with experimental observation. It indicates that the forces produced by ECH could change the toroidal flow velocity.

We have solved the diffusion equation to evaluate the toroidal flow velocity by NBI heating and ECH, and compared the results with two LHD experiments. In the balanced NBI heating case, we obtained a reasonable agreement in the flow velocity. In the co-rotating plasma, we obtain the change of toroidal flow velocity, which agrees with the experiments qualitatively. However, the counter directed force by ECH is less than that of the co directed force by NBI heating. Therefore, we cannot reproduce the flow entirely.

The toroidal flow calculations have been done with a rough estimation of viscosity, so we have to make more precise predictions in future work. Especially the plasma flow has been considered to move primarily along the helical ripple experimentally and theoretically[31–34]. In helical plasmas, the $E \times B$ flow is almost in the poloidal direction and the toroidal component of $E \times B$ flow is quite small in the core region. The same is true for the experiments referred in this paper. Also, the flow direction is sometimes opposite to the $E_r \times B_\theta$ flow direction due to the neoclassical parallel viscosity[32]. Therefore we are tackling to introduce the more precise neoclassical viscosity effect. Also, the residual stress caused by turbulence can generate flow shear, and it can be a promising candidate of the driving force to explain the difference of the co NBI heating case[3,35–37].

ACKNOWLEDGMENTS

The authors thank LHD Experiment Group for their excellent support of this work. This work was supported by JSPS KAKENHI Grant Numbers JP18K03582. This work was also supported by the National Institute for Fusion Science grant administrative budget (NIFS10ULHH021) and the NIFS Collaboration Research program (NIFS19KNST150). This work was also supported by the Ministry of Science and ICT under KFE R&D Program of "KSTAR Experimental Collaboration and Fusion Plasma Research(KFE-EN2101-12)".

DATA AVAILABLITY

The data that support the findings of this study are available from the corresponding author upon reasonable request.

[1] M. Yoshida, Y. Kamada, H. Takenaga, Y. Sakamoto, N. Oyama, H. Urano and the JT-60 Team, Nucl. Fusion **49** 115028 (2009).
[2] S.T.A. Kumar, J.N. Talmadge, T.J. Dobbins, F.S.B. Anderson, K.M. Likin and D.T. Anderson, Nucl. Fusion, **57** 036030 (2017).
[3] P. H. Diamond, Y. Kosuga, Ö.D. Gürcan,C.J. McDevitt, T.S. Hahm, N. Fedorczak, J.E. Rice, W.X. Wang, S. Ku, J.M. Kwon, *et al.,* , Nucl. Fusion **53** 104019 (2013).
[4] M. Yoshinuma, K. Ida, M. Yokoyama, M. Osakabe and K. Nagaoka, Fusion Science and Technology **58** 375 (2010).
[5] K. Ida, S. Kado, and Y. Liang, Rev. Sci. Instrum. **71** 2360 (2000).
[6] K. Nagaoka, K. Ida, M. Yoshinuma, Y. Takeiri, M. Yokoyama, S. Morita, K. Tanaka, T. Ido, A. Shimizu, N. Tamura, *et al.,* Nucl. Fusion **51** 083022 (2011).
[7] K. Nagaoka, K. Ida, M. Yoshinuma, Y. Suzuki, K. Kamiya, S. Satake, K. Tanaka, M. Yokoyama, S. Murakami, M. Osakabe, *et al.,* Phys. Plasmas **20** 056116 (2013).
[8] K. Ida, Y. Sakamoto, M. Yoshinuma, H. Takenaga, K. Nagaoka, N. Hayashi, N. Oyama, M. Osakabe, M. Yokoyama, H. Funaba, *et al.,* Nucl. Fusion **49** 095024 (2009).
[9] K. Ida and T. Fujita, Plasma Phys. Control. Fusion **60** 033001 (2018).
[10] M.N. Rosembluth and F.L. Hinton, Nucl. Fusion, **36** 55 (1996).
[11] A. Snicker, O. Asunta, H. Ylitie, T. Kurki-Suonio, M. Schneider and S.D. Pinches, Nucl. Fusion **55** 063023 (2015).
[12] M. Honda, T. Takizuka, A. Fukuyama, M. Yoshida and T. Ozeki, Nucl. Fusion **49** 035009 (2009).
[13] V.S. Chan, S.C. Chiu, and Y.A. Omelchenko, Phys. Plasmas **9**, 501 (2002).
[14] Y. Yamamoto, S. Murakami, C.C. Chang, S.T.A. Kumar, J.N. Talmadge, K. Likin and D.T. Anderson, Plasma Fusion Res. **14**, 3403105 (2019).
[15] S. Murakami, U. Gasparinoa, H. Idei, S. Kubo, H. Maassberg, N. Marushchenko, N. Nakajima, M. Romé, M. Okamoto, Nucl. Fusion **40** 693 (2000).
[16] J. Chen, K. Ida, M. Yoshinuma, T. Kobayashi, S. Murakami, Y. Yamamoto, M.Y. Ye, and B. Lyu, Nucl. Fusion **59** 106036 (2019).
[17] S. Nishimura, K. Ida, M. Osakabe, T. Minami, K. Tanaka, and CHS Group, Physics of Plasmas, **7** 437 (2000).
[18] J. Arévalo, J.A. Alonso, K.J. McCarthy and J.L. Velasco, Nucl. Fusion **53** 023003 (2013).
[19] Y. Yamamoto, S. Murakami, H. Takahashi, K. Ida, M. Yoshinuma, and J. Chen, Phys. Plasmas **27** 042514 (2020).
[20] K.C. Shaing and J.D. Callen, Phys. Fluids **26** 3315 (1983).
[21] M. Romé V. Erckmann, U. Gasparino, H.J. Hartfuß, GKüher, H. Maaßberg and N. Marushchenko Plasma Phys. Control. Fusion **39** 117 (1997).
[22] S. Hasegawa, S. Murakami and Y. Moriya, Plasma and Fusion Research **8** 2403083 (2013).
[23] S. Murakami, N. Nakajima and M. Okamoto, Trans. Fusion Technol. **27** 256 (1995).
[24] S. Murakami, H. Yamaguchi, A. Sakai, A. Wakasa, A. Fukuyama, K. Nagaoka, H. Takahashi, H. Nakano, M. Osakabe, K. Ida, *et al.,* Plasma Phys. Control. Fusion **57** 054009 (2015).

[25] A. Wakasa, S. Murakami and S. Oikawa, Plasma and Fusion Research, **3** S1030 (2008).
[26] A. Wakasa, A. Fukuyama, S. Murakami, M. Miki, M. Yokoyama, M. Sato, S. Toda, H. Funaba, K. Tanaka, K. Ida, *et al.,* Integrated transport simulation of LHD plasmas using TASK3D, IAEA THC/P4-29 (2010).
[27] K. Ida, Plasma Phys. Control. Fusion **40** 1429 (1998)
[28] K. Ida, M. Yoshinuma, K. Yamasaki, T. Kobayashi, Y. Fujiwara, Y. Yamamoto, S. Murakami, and M. Kobayashi, Rev. Sci. Instrum. **90** 093503 (2019).
[29] J. Beckers, K. Ida, M. Yoshinuma, M. Emoto, R. Seki, M. Yokoyama and R. Jaspers Plasma Fusion Res. **12** 1402006 (2017).
[30] K. Ida, H. Lee, K. Nagaoka, M. Osakabe, C. Suzuki, M. Yoshinuma, R. Seki, M. Yokoyama, T. Akiyama, and LHD Experiment Group Phys. Rev. Lett. **111** 055001 (2013).
[31] M. Yoshinuma, K. Ida, M. Yokoyama, K. Nagaoka, M. Osakabe and the LHD Experimental Group, Nucl. Fusion **49** 075036 (2009).
[32] K. Ida, T. Minami, Y. Yoshimura, A. Fujisawa, C. Suzuki, S. Okamura, S. Nishimura, M. Isobe, H. Iguchi, K. Itoh, *et al.,* Phys. Rev. Lett. **86**, 3040 (2001).
[33] D.A. Spong Phys. Plasmas **12** 056114 (2005).
[34] A. Briesemeister, K. Zhai, D.T. Anderson, F.S.B. Anderson, J. Lore, and J.N. Talmadge, Contrib. Plasma Phys. **50** 741 (2010).
[35] K. Ida, M. Yoshinuma, K. Nagaoka, M. Osakabe, S. Morita, M. Goto, M. Yokoyama, H. Funaba, S. Murakami, K. Ikeda, *et al.,* Nucl. Fusion **50** 064007 (2010).
[36] J.M. Kwon, S. Yi, T. Rhee, P.H. Diamond, K. Miki, T.S. Hahm, J.Y. Kim, Ö.D. Gürcan and C. McDevitt Nucl. Fusion **52** 013004 (2012).
[37] K. Ida and J.E. Rice, Nucl. Fusion **54** 045001 (2014).